

# Flexible Thermoelectric Devices of Ultrahigh Power Factor by Scalable Printing and Interface Engineering

Tony Varghese, Chaochao Dun, Nicholas Kempf, Mortaza Saeidi-Javash, Chinnathambi Karthik, Joseph Richardson, Courtney Hollar, David Estrada, and Yanliang Zhang\*

Printing is a versatile method to transform semiconducting nanoparticle inks into functional and flexible devices. In particular, thermoelectric nanoparticles are attractive building blocks to fabricate flexible devices for energy harvesting and cooling applications. However, the performance of printed devices are plagued by poor interfacial connections between nanoparticles and resulting low carrier mobility. While many rigid bulk materials have shown a thermoelectric figure of merit  $ZT$  greater than unity, it is an exacting challenge to develop flexible materials with  $ZT$  near unity. Here, a scalable screen-printing method to fabricate high-performance and flexible thermoelectric devices is reported. A tellurium-based nanosolder approach is employed to bridge the interfaces between the BiSbTe particles during the postprinting sintering process. The printed BiSbTe flexible films demonstrate an ultrahigh room-temperature power factor of  $3 \text{ mW m}^{-1} \text{ K}^{-2}$  and  $ZT$  about 1, significantly higher than the best reported values for flexible films. A fully printed thermoelectric generator produces a high power density of  $18.8 \text{ mW cm}^{-2}$  achievable with a small temperature gradient of  $80 \text{ }^\circ\text{C}$ . This screen-printing method, which directly transforms thermoelectric nanoparticles into high-performance and flexible devices, presents a significant leap to make thermoelectrics a commercially viable technology for a broad range of energy harvesting and cooling applications.

## 1. Introduction

The thermoelectric (TE) field has seen significant progress in increasing the figure of merit ( $ZT$ ) in the past two decades. Their solid-state and compact nature makes thermoelectric generators (TEGs) produced from such high  $ZT$  materials a promising technology for capturing waste heat and boosting energy efficiency. Despite considerable  $ZT$  increases in the past two decades realized via nanostructuring and other techniques,<sup>[1–7]</sup> a huge chasm still remains to make TEGs a cost-competitive and commercially viable technology for a broad range of applications. The conventional TEG manufacturing process is expensive and inflexible, which is not adaptable for different applications. Advances in manufacturing methods are thus a paramount need to transform high-efficiency nanostructured materials into cost-effective devices in order to realize the highly anticipated impact of thermoelectric technology. Printing techniques, such as direct writing,<sup>[8–10]</sup> inkjet printing,<sup>[11,12]</sup> and screen printing,<sup>[13–16]</sup> have shown promise as scalable and cost-

effective fabrication processes to realize flexible electronic and thermoelectric devices.<sup>[17,18]</sup> Among them, screen printing is a highly scalable, efficient, and low-cost technique to manufacture flexible thermoelectric devices.


Flexible thermoelectric generators (f-TEGs) have attracted great attention in recent years because of their broad range of applications as power sources for flexible electronics and wearable devices, which have rapidly growing markets.<sup>[11,19–24]</sup> Research progresses on flexible TE materials and devices, including conducting polymers,<sup>[25]</sup> nanocomposites comprised of inorganic nanostructures in polymer matrices,<sup>[26–28]</sup> and fully inorganic flexible thin films<sup>[20,24]</sup> have been reported previously.<sup>[29]</sup> The exponential growth in the Internet of Things demands a large-scale, affordable, and uninterrupted power supply. Compared with other potential power sources, such as solar and piezoelectric devices, f-TEGs can continuously generate electricity from body/ambient thermal energy without the need for mechanical motion or sunlight.<sup>[30,31]</sup> Nevertheless, the low thermoelectric power factor of printed flexible films

Dr. T. Varghese, Dr. C. Karthik, Prof. D. Estrada  
Micron School of Materials Science and Engineering  
Boise State University  
Boise, ID 83725, USA

Dr. C. Dun, N. Kempf, M. Saeidi-Javash, Prof. Y. Zhang  
Department of Aerospace and Mechanical Engineering  
University of Notre Dame  
Notre Dame, IN 46556, USA  
E-mail: yzhang45@nd.edu

J. Richardson  
Department of Electrical and Computer Engineering  
Boise State University  
Boise, ID 83725, USA

Dr. C. Hollar  
Department of Mechanical and Biomedical Engineering  
Boise State University  
Boise, ID 83725, USA

 The ORCID identification number(s) for the author(s) of this article can be found under <https://doi.org/10.1002/adfm.201905796>.

DOI: 10.1002/adfm.201905796

compared with that of their rigid and bulk counterparts remains a major obstacle in applying f-TEGs in a broad range of energy harvesting and cooling applications.<sup>[32]</sup> Moreover, there exist limited sintering options for the films printed on flexible substrates, leading to the formation of undesirable pores and thus reduced electrical conductivity.<sup>[12,33]</sup> Recently, attempts have been made to improve the electrical conductivity of TE materials fabricated from nanocrystals using composition-matched molecular solders,<sup>[34,35]</sup> but this method is not compatible with scalable printing at ambient conditions due to the complicated chemical synthesis involving hydrazine.

Here, we report a highly scalable and low-cost screen-printing process to fabricate flexible and high-performance p-type films using ball-milled  $\text{Bi}_{0.4}\text{Sb}_{1.6}\text{Te}_3$  nanoparticles. A nanosolder-assisted sintering process with additional tellurium particles was successfully employed to bridge the interfaces of TE particles, which significantly improve charge carrier mobility of the printed films. The printed films demonstrate a thermoelectric power factor of  $3 \text{ mW m}^{-1} \text{ K}^{-2}$  and  $ZT$  about 1 at room temperature accompanied by superior flexibility, which is unprecedented for flexible films. A functional f-TEG was fabricated that exhibits a power density of  $18.8 \text{ mW cm}^{-2}$  at a temperature difference of  $80 \text{ }^\circ\text{C}$ .

## 2. Results and Discussion

High-energy ball-milled  $\text{Bi}_{0.4}\text{Sb}_{1.6}\text{Te}_3$  (BST) nanoparticles<sup>[36]</sup> were used to synthesize printable thermoelectric ink. The fabrication process for a f-TEG using scalable and low-cost screen printing and nanosolder-assisted sintering is shown in **Figure 1**. The detailed fabrication process is discussed in the Experimental Section below.

**Figure 2a,b** shows the comparison between a scanning electron microscopy (SEM) images of the printed BST film with

8 wt% addition of tellurium particles (BST:T) and that of a pure BST film after sintering at  $450 \text{ }^\circ\text{C}$ . It is clear that the BST:T sample has denser structures with larger grain size and fewer pores. **Figure 2a,c** shows the Te-rich areas in the BST:T film, as compared with the uniform distribution of Bi, Sb, and Te in the pure BST film shown in **Figure 2b,d**. Elemental ratio analysis of the main phase of each film reveals the Bi:Sb:Te element ratio to be 0.4:1.6:3, while the Te-rich areas in the BST:T film are dominated by the reprecipitation of tellurium with Te element ratio exceeding 88%. Details of the energy-dispersive X-ray spectroscopy (EDS) analysis are provided in **Figure S1** (Supporting Information), with SEM in lower magnification given in **Figure S2** (Supporting Information). In addition, X-ray diffraction pattern comparison between BST and BST:T samples (shown in **Figure S3** in the Supporting Information) verifies the presence of excess elemental tellurium in the BST:T sample, which is in agreement with the EDS. During the sintering process at  $450 \text{ }^\circ\text{C}$ , the excess tellurium particles, with melting temperature  $< 449 \text{ }^\circ\text{C}$ , creates a liquefied tellurium phase in the solid BST matrix, which acts as a coalescing agent to facilitate the consolidation and interfacial connection between BST particles.

Transmission electron microscope (TEM) images in **Figure 3** show the segregation and precipitation of liquid-phase Te in the area between BST grains, which acts like a “glue” filling in the voids in the printed BST:T film. The compositions of the grains across the interface were confirmed by quantitative spot EDS analysis performed on the grain boundary region (part I) and bulk BST grain (part II), indicating almost 96 at% Te at the intergrain region. An EDS line scan across the Te–BST interface indicates almost pure Te element on the Te side and a mixture of Bi–Sb–Te elements on the BST side (**Figure 3d**). A closer look at the interface region using lattice imaging (**Figure 3b**) reveals the presence of nanocrystalline Te, as indicated by the lattice and Moiré fringes in the overlapping areas, indicating the crystallization of molten Te when the sample was cooled down

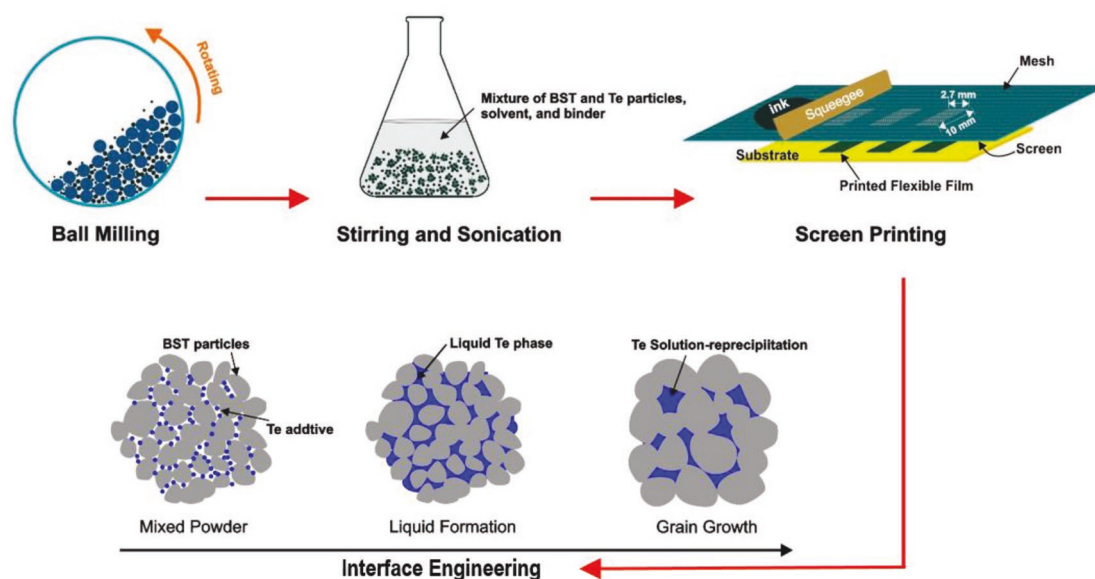


**Figure 1.** Converting  $\text{Bi}_{0.4}\text{Sb}_{1.6}\text{Te}_3$  (BST) nanoparticle ink into a flexible thermoelectric generator using a scalable and low-cost screen-printing process and nanosolder-assisted interface engineering.

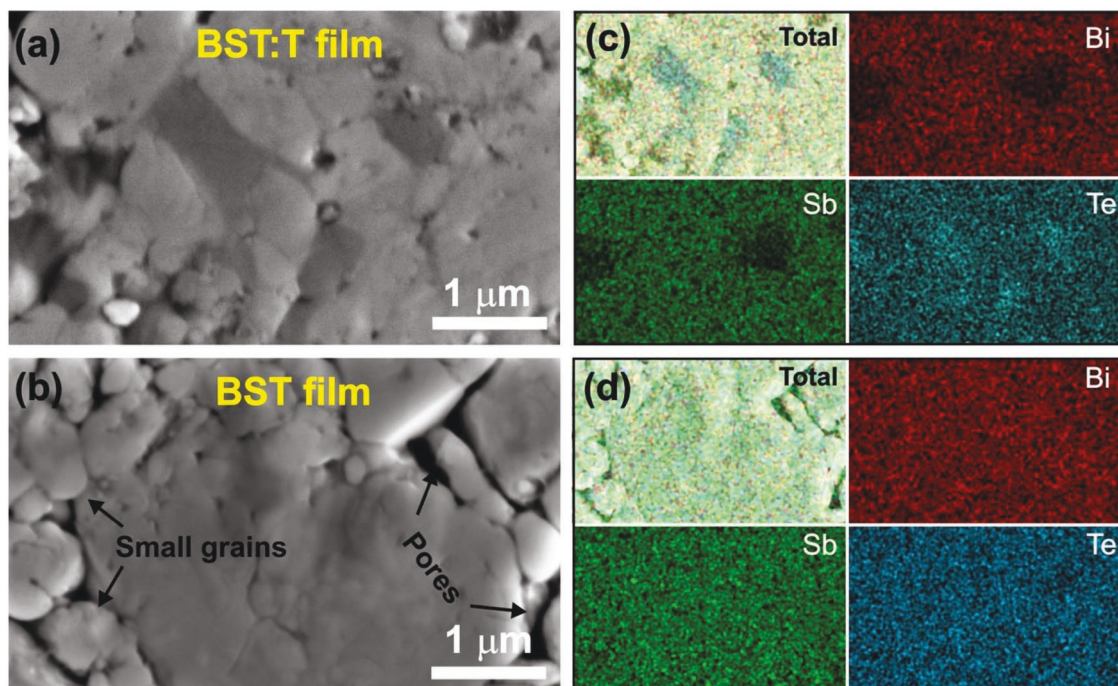


**Figure 2.** SEM images of a) printed Bi<sub>0.4</sub>Sb<sub>1.6</sub>Te<sub>3</sub> films with 8 wt% Te and b) printed pure Bi<sub>0.4</sub>Sb<sub>1.6</sub>Te<sub>3</sub> films after sintering. c,d) The corresponding EDS mapping is given, respectively.

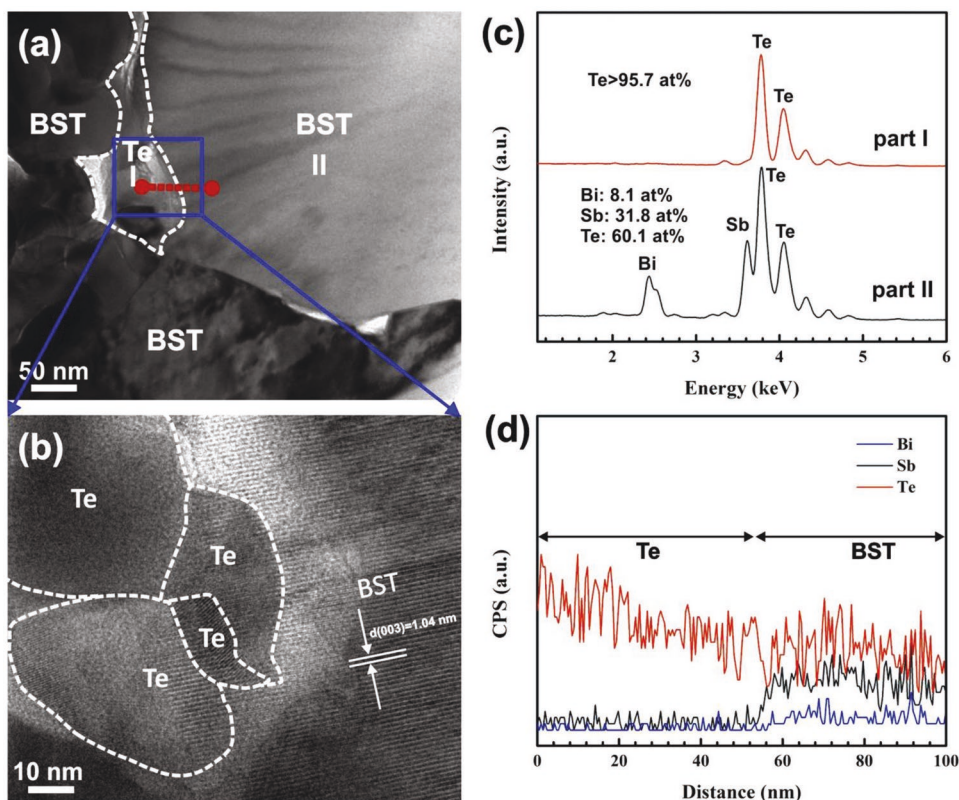


**Figure 3.** a) Bright-field TEM image of BST:T specimen, showing the presence of pure Te in the intergrain region highlighted using dotted lines. b) Lattice-resolved HRTEM image of the intergrain region, revealing the nanocrystalline nature of the segregated Te. c) EDS analysis of part I and part II marked in (a). d) EDS line scan performed along the region marked with a red dotted line in (a), showing the variation of Te and other elements across the BST and Te interface.

below the sintering temperature. In addition to these nanocrystalline Te filling in the nanosized voids between BST grains, some Te grains of larger sizes were observed near the surfaces of the BST:T film, which were likely formed when a fraction of the excess liquid-phase Te was expelled toward the surfaces of the film during the sintering process (Figure S6, Supporting Information). For comparison, TEM analysis of pure BST films with no extra Te does not show the presence of pure Te grains or segregates (Figure S7, Supporting Information).

Temperature-dependent thermoelectric properties were systematically studied based on printed films with an average thickness around 27  $\mu\text{m}$ . As shown in Figure 4a, both BST and BST:T systems show decreased electrical conductivity with increased temperature, which is consistent with their semimetallic nature. The room-temperature electrical conductivity of the BST:T film is 42% higher than that of the BST film. It is believed that the tellurium addition results in: I) diminished carrier scattering due to improved interfacial connections between BST particles, and II) an increased carrier (hole) concentration consistent with previous reports, which is closely related to the modulation of antisites ( $\text{Sb}_{\text{Te}^-}$  and  $\text{Bi}_{\text{Te}^-}$ ) and anion vacancy ( $\text{V}_{\text{Te}^{2+}}$ ) defects in the BST matrix.<sup>[37,38]</sup> In order to confirm the change of carrier concentration and mobility, room-temperature Hall measurements were performed on a series of flexible films. An increased carrier concentration from  $2.4 \times 10^{19}$  to  $3.1 \times 10^{19} \text{ cm}^{-3}$ , as well as an increased carrier mobility from 111.4 to  $135.9 \text{ cm}^2 \text{ V}^{-1} \text{ s}^{-1}$ , were observed

in the BST:T film as compared with the BST film. Normally, the carrier mobility is insensitive to such a small change of carrier concentration, as observed in the bulk BiSbTe materials.<sup>[39]</sup> However, the introduction of additional Te in the BST:T system could be conducive to the synergistic effect of increased carrier concentration accompanied by the suppressed scattering of charge carriers. Specifically, it is believed that the excess Te particles create a liquefied tellurium phase in the solid BST matrix, which acts as a coalescing agent to facilitate the consolidation of the BST nanoparticles. As a result, the melted tellurium at the BST interfaces improves the network between the BST particles and thus increases the carrier mobility due to reduced film porosity and diminished carrier scattering at the pore boundaries.<sup>[35]</sup> Therefore, the simultaneously improved carrier concentration and mobility finally gives rise to the enhanced electrical conductivity in the printed BST:T film, approaching that of the bulk BST counterpart.

With the tellurium addition, the Seebeck coefficient of the BST:T films decreases slightly from 230 to  $204 \mu\text{V K}^{-1}$ , as shown in Figure 4b. The reduced Seebeck coefficient is associated with the increased charge-carrier concentration as discussed above. At the same time, the Seebeck coefficient of BST:T films first increases and then starts to decrease at the higher temperature of 150  $^\circ\text{C}$  as compared with 105  $^\circ\text{C}$  for pure BST films. This is because the excess tellurium reduces the density of positively charged tellurium vacancies (minority carriers),<sup>[35]</sup> decreasing the extent of the bipolar effect, which is in agreement with

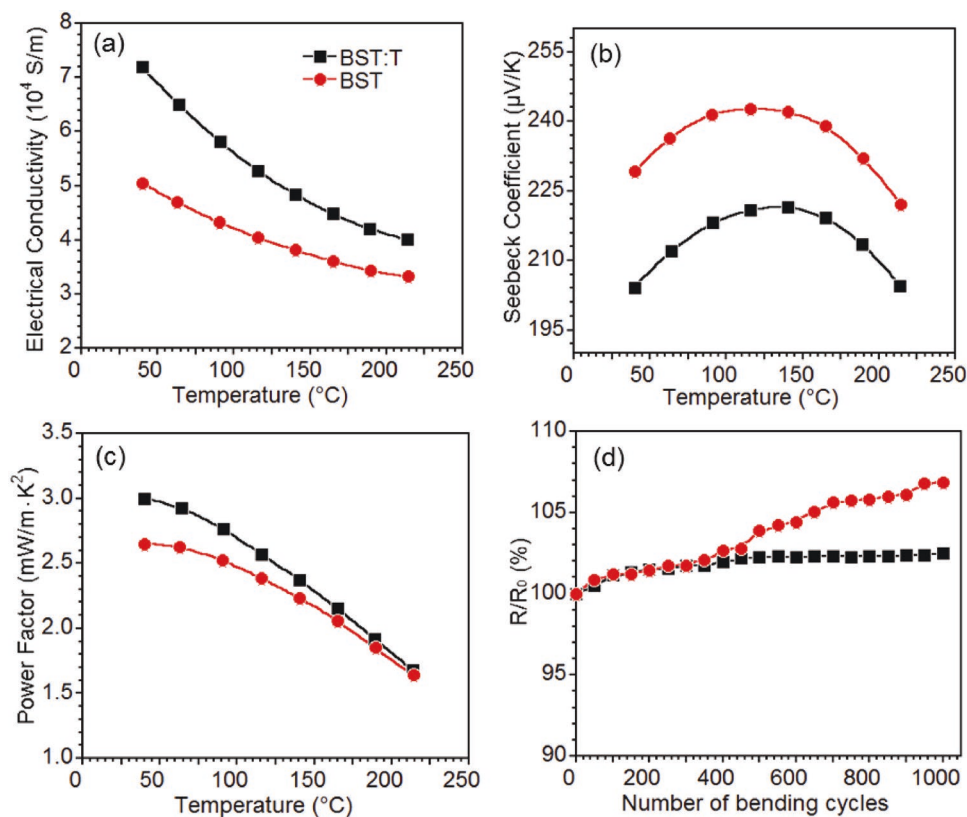


**Figure 4.** Temperature-dependent a) electrical conductivity, b) Seebeck coefficient, and c) power factor of both BST and BST:T films. d) Normalized resistance of flexible films versus number of bending cycles with a 10 mm bending radius for both BST and BST:T films. Here,  $R_0$  and  $R$  are the resistances before and after bending.

the Hall-measurement results. Figure 4c shows that the room-temperature power factor of the BST:T film is 13% higher than that of the pure BST film due to its significantly increased electrical conductivity. The room-temperature thermal conductivity of the BST:T film and the BST film were determined to be 0.9 and 0.95 W m<sup>-1</sup> K<sup>-1</sup> using the Angstrom method. This results in a room-temperature *ZT* value about 1 for the BST:T films, which is significantly higher than the previous best reported *ZT* values of flexible films, as shown in Table 1. The thermal conductivity of the BST:T film is slightly lower than the BST film because the secondary tellurium phase presented in the BST:T film increases phonon scattering and thus reduces the lattice thermal conductivity  $\kappa_L$ . The  $\kappa_L$  of the BST:T film and the BST film is calculated to be 0.62 and 0.74 W m<sup>-1</sup> K<sup>-1</sup> using the Lorenz number extracted from previous report.<sup>[36]</sup> Table 1 summarizes the room-temperature power factor and *ZT* values of several p-type flexible films fabricated by different methods, showing that BST:T has the highest reported values thus far in both categories. The room-temperature power factor of our printed BST:T films reaches 3 mW m<sup>-1</sup> K<sup>-2</sup>, which is significantly higher than the dispenser-printed and inkjet-printed BiSbTe films of similar compositions due to orders of magnitude increased electrical conductivity. Screen-printing method used in this work offers a high TE particle loading in the ink, minimizing the solvent and other parasitic additives and thereby increasing the density and electrical conductivity of the

**Table 1.** Comparison of room-temperature thermoelectric performance between this work and previous best reported values of p-type flexible thermoelectric films.

Composition	Power factor [mW m <sup>-1</sup> K <sup>-2</sup> ]	<i>ZT</i>	Fabrication method	Ref.
BiSbTe + 8 wt% Te	3.0	1	Screen printing	This work
BiSbTe	0.06	n/a	Inkjet printing	[11]
BiSbTe	0.18	0.2	Direct write	[10]
p-type Bi <sub>2</sub> Te <sub>3</sub> /poly(3,4-ethylenedioxythiophene) hybrid	1.35	0.58	Evaporation	[40]
Doped carbon nanotube	0.7	0.1	Spray coating	[41]
Hybrid complex	0.06	0.3	Drop casting	[42]
Doped poly(3,4-ethylenedioxythiophene)	0.45	0.42	Spin casting	[43]
CuI	0.4	0.21	Sputtering	[44]
Ca <sub>3</sub> Co <sub>4</sub> O <sub>9</sub>	0.23	n/a	Sputtering	[45]

printed films. Furthermore, the optimized sintering condition with the addition of the Te particles improves interfacial connections and carrier mobility of the printed TE films.

In order to test the flexibility of the printed films, the room-temperature electrical resistance was tested using a van der Pauw method as a function of bending cycles with a 10 mm bending

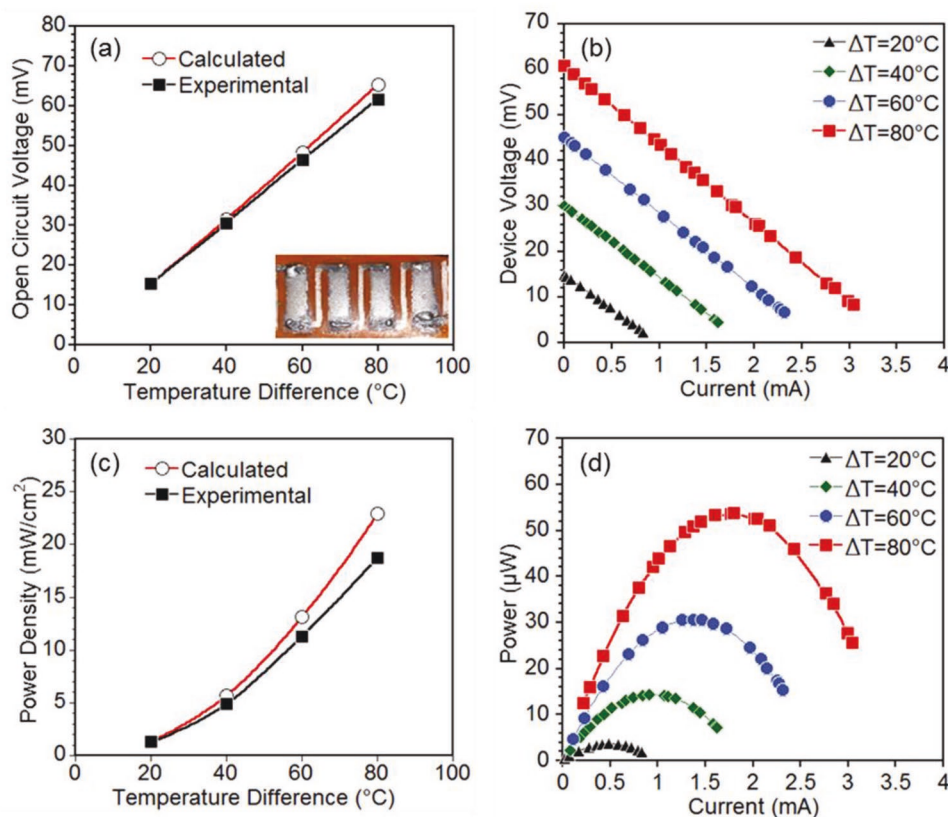


**Figure 5.** Performance of a flexible TE device fabricated by screen-printing process: a) calculated and experimental open-circuit voltage versus temperature differences ( $\Delta T$ ) (inset: photo of the printed device), b) device operating voltage versus current tested at various  $\Delta T$ , c) calculated and experimental electrical power density tested at various  $\Delta T$ , and d) power output versus electrical current at various  $\Delta T$ .

radius. Electrical resistance was chosen to evaluate the film flexibility because it is highly sensitive to any cracks that may develop during bending test. As shown in Figure 4d, the BST:T film and the BST film show 3% and 7% increases in resistance, respectively, after 1000 bending cycles, indicating the superior flexibility of the printed film with the nanosolders. No noticeable changes of Seebeck coefficient were observed before and after bending.

Finally, a  $\mu$ -TEG consisting of four BST:T TE elements (shown in the inset of Figure 5a) was printed, and tested at various temperature differences ( $\Delta T$ ) with the hot side varying in the range of 40–100 °C and the cold side maintained at 20 °C. Figure 5a shows that the experimentally measured device open-circuit voltage linearly increases with  $\Delta T$  by virtue of the Seebeck effect, which agrees with the calculated results within 5% at 80 °C  $\Delta T$ . Figure 5b,d shows the device operating voltage and power output, respectively, as a function of electrical current tested at different  $\Delta T$ . A maximum power output of 54  $\mu$ W was obtained with a  $\Delta T$  of 80 °C when the external load resistance matches the internal resistance of the device. The device power density increases with  $\Delta T$  and reaches 18.8 mW cm<sup>-2</sup> at 80 °C  $\Delta T$ , as shown in Figure 5c. It should be noted that the power density is one of the most important criteria to evaluate the performance of TEG energy harvesters. Here, the power density was evaluated based on the total cross-sectional area of the four thermoelectric elements perpendicular to the heat flow direction. The differences between the experimental power density and the calculated values increases slightly with  $\Delta T$  due to the increasing electrical contact resistances at the junctions between the metal electrodes and the TE elements. The average contact resistance of the device is determined to be about 0.9  $\Omega$  at room temperature. The fully printed flexible thermoelectric generator with a power density of 18.8 mW cm<sup>-2</sup> at 80 °C  $\Delta T$  is sufficient to power the Internet of things and sensors with typical power consumptions from 100 nW to 100 mW.<sup>[46]</sup> The screen-printed thermoelectric devices based on flexible films have potential to significantly reduce thermoelectric materials cost compared with bulk devices with TE element thicknesses of millimeters due to reduced material consumptions. In addition, the direct conversion of thermoelectric particles into devices realized by the screen-printing process not only eliminates materials waste but also reduces manufacturing cost compared with conventional device manufacturing method which typically involves numerous processes such as powder hot press, polishing, dicing, and assembling and joining TE elements with metal electrodes.<sup>[47]</sup>

### 3. Conclusion

In conclusion, flexible BiSbTe-based thermoelectric devices were fabricated using a highly scalable and low-cost screen-printing method. A bulk-like power factor of 3 mW m<sup>-1</sup> K<sup>-2</sup> and a  $ZT$  about 1 were achieved at room temperature, which is significantly higher than previous reported values of flexible TE films and is ideal for near room-temperature energy harvesting applications. Bending test revealed excellent flexibility of the printed films, which exhibit only a 3% increase in electrical resistance after 1000 bending cycles on a 10 mm radius cylinder. The flexible thermoelectric device fabricated using

printed BiSbTe films and silver electrodes exhibits an exceptional power density of 18.8 mW cm<sup>-2</sup> at a relatively small temperature difference of 80 °C. The flexible, high-performance, and low-cost thermoelectric devices demonstrated in this work present a significant leap in the field of thermoelectrics toward a commercially viable technology for a broad range of energy-harvesting and thermal-management applications.

### 4. Experimental Section

It was determined that a small amount of tellurium particles could be mixed with the Bi<sub>0.4</sub>Sb<sub>1.6</sub>Te<sub>3</sub> particles to facilitate sintering and help connect the Bi<sub>0.4</sub>Sb<sub>1.6</sub>Te<sub>3</sub> particles. The tellurium particles melted during sintering when the temperature was above its melting point but below the BST melting point. A suitable amount of TE powder was weighed and mixed with a measured amount of solvent and binder. Here, the optimized ink contained 84 wt% TE particles, 13 wt% solvent ( $\alpha$ -Terpineol, Sigma-Aldrich), and 3 wt% binder (Disperbyk-110, BYK USA Inc.). The ink was well mixed using a planetary centrifugal mixer for 20 min followed by a vortex mixer for 10 min to obtain uniformity.

The TE ink was printed onto a 51  $\mu$ m thick HN-Kapton substrate using 180 mesh screens. Before printing, Kapton films were cut to required dimensions and cleaned using methanol and isopropanol by sonication. Multiple passes of printing were applied to obtain the desired film thickness and uniformity. Freshly printed films were allowed to rest for 30 min in their initial state, allowing reduction of the mesh pattern on the films. The printed films were then dried at 200 °C for 30 min in a nitrogen environment in order to remove the solvent and binder. The dried samples were further densified using a hydraulic press with pressure up to 200 MPa. Finally, the pressed films were sintered at 450 °C for 45 min using a tube furnace under inert environment. The sintering temperature was kept below the melting point of the Kapton substrate.

In order to fabricate a thermoelectric device, a series of sintered films were electrically connected using screen-printed silver contacts (HPS-FG57B silver ink, Novacentrix) and flash-dried at 350 °C for 1 min. A completely printed device was fabricated using four thermoelectric elements with 27  $\mu$ m thickness connected by silver prints. The total weight of the printed thermoelectric generator with electrical contacts was under 19 mg. The thickness, microstructure, and elemental compositions of the films were characterized using field emission-scanning electron microscopy (Teneo) equipped with EDS.

The temperature-dependent in-plane electrical conductivity and Seebeck coefficient of the film were measured using a commercial Linseis Seebeck and resistivity instrument (LSR system, Germany). The measurement uncertainties of the LSR were less than 2% for the electrical conductivity and less than 3% for the Seebeck coefficient, respectively. The Hall measurement was conducted on a modified Hall Effect measurement system (Ecopia HMS5000/AMP55T) at a permanent magnetic field of 0.545 T in a van der Pauw configuration. The room-temperature thermal conductivity  $k$  of the printed films was determined through the measurement of the thermal diffusivity  $\alpha$ , specific heat capacity  $c_p$ , and density  $\rho$ , using the relationship  $k = \alpha \rho c_p$ . Thermal diffusivity was measured using the Angstrom method (Figure S8, Supporting Information) by applying a sinusoidal heat signal at one end of the sample and measuring the temperature response as a function of time at two different locations along the sample. The thermoelectric device was measured using a custom-built testing system with controlled hot-side and cold-side temperatures, and a variable resistor to match the TE device resistances in order to obtain the maximum power output.

The crystallization of all films was analyzed by X-ray diffraction using Cu  $K\alpha$  radiation ( $\lambda = 1.5418$  Å, Bruker D2 Phaser). Scanning electron microscopy (SEM) and related EDS tests were performed using Magellan 400 (FEI Company), with working voltage 15 KV and working distance 4.5 mm. TEM specimens of BST:T film were prepared using both focused ion beam (FIB) milling and conventional ion milling process. For the first

one, a FEI Helios FIB-SEM (FEI Company, Hillsboro, OR, USA) was used for serial sectioning and data collection. For the latter, the films were initially punched to 3 mm diameter disks using a Gatan 659 disk punch. These disks were then attached to copper aperture grids (Ted Pella Inc.) for support with the film side down using Epotek 350ND epoxy. Once the epoxy was cured, the Kapton substrate was peeled off leaving behind only the BST:T film attached to the support grid. The sample was then ion milled using a Gatan 691 precision ion polishing system until perforation. Bright-field, high resolution (HR) transmission lattice imaging (HRTEM) and EDS were carried out using a JEOL 2100 HRTEM fitted with an Oxford Instruments X-MAX 80 TLE EDS spectrometer.

## Supporting Information

Supporting Information is available from the Wiley Online Library or from the author.

## Acknowledgements

T.V. and C.D. contributed equally to this work. Y.Z. acknowledges funding support from the National Science Foundation under Award CMMI-1747685, the Defense Advanced Research Projects Agency under Award DARPA HR00111820030, and the U.S. Department of Energy under Awards DE-NE0008712 and DE-NE0008812. D.E. acknowledges support from the National Aeronautics Space Administration under Award 80NSSC17M0029. The authors thank Dr. Zhifeng Ren and Dr. Dezhi Wang at the University of Houston for providing the TE powders for this study. The authors also thank Dr. Paul Smeets at the Northwestern University for his support on FIB and TEM experiments.

## Conflict of Interest

The authors declare no conflict of interest.

## Keywords

flexible thermoelectrics, interface engineering, nanosolder, screen printing

Received: July 17, 2019

Revised: October 17, 2019

Published online:

- [1] G. Tan, L. D. Zhao, M. G. Kanatzidis, *Chem. Rev.* **2016**, *116*, 12123.
- [2] K. Biswas, J. He, I. D. Blum, Chun-IWu, T. P. Hogan, D. N. Seidman, V. P. Dravid, M. G. Kanatzidis, *Nature* **2012**, *489*, 414.
- [3] L.-D. Zhao, S.-H. Lo, Y. Zhang, H. Sun, G. Tan, C. Uher, C. Wolverton, V. P. Dravid, M. G. Kanatzidis, *Nature* **2014**, *508*, 373.
- [4] A. J. Minnich, M. S. Dresselhaus, Z. F. Ren, G. Chen, *Energy Environ. Sci.* **2009**, *2*, 466.
- [5] R. J. Mehta, Y. Zhang, C. Karthik, B. Singh, R. W. Siegel, T. Borca-Tasciuc, G. Ramanath, *Nat. Mater.* **2012**, *11*, 233.
- [6] P. Jood, M. Ohta, A. Yamamoto, M. G. Kanatzidis, *Joule* **2018**, *2*, 1339.
- [7] L. Sun, B. Liao, D. Sheberla, D. Kraemer, J. Zhou, E. A. Stach, D. Zakharov, V. Stavila, A. A. Talin, Y. Ge, M. D. Allendorf, G. Chen, F. Léonard, M. Dincă, *Joule* **2017**, *1*, 168.
- [8] M. Gao, L. Li, W. Li, H. Zhou, Y. Song, *Adv. Sci.* **2016**, *3*, 1600120.
- [9] D. Madan, A. Chen, P. K. Wright, J. W. Evans, D. Madan, A. Chen, P. K. Wright, J. W. Evans, *J. Appl. Phys.* **2011**, *109*, 034904.
- [10] D. Madan, Z. Wang, A. Chen, P. K. Wright, J. W. Evans, *ACS Appl. Mater. Interfaces* **2013**, *5*, 11872.
- [11] Z. Lu, M. Layani, X. Zhao, L. P. Tan, T. Sun, S. Fan, Q. Yan, S. Magdassi, H. H. Hng, *Small* **2014**, *10*, 3551.
- [12] T. Juntunen, H. Jussila, M. Ruoho, S. Liu, G. Hu, T. Albrow-Owen, L. W. T. Ng, R. C. T. Howe, T. Hasan, Z. Sun, I. Tittonen, *Adv. Funct. Mater.* **2018**, *28*, 1800480.
- [13] C. Han, G. Tan, T. Varghese, M. G. Kanatzidis, Y. Zhang, *ACS Energy Lett.* **2018**, *3*, 818.
- [14] T. Varghese, C. Hollar, J. Richardson, N. Kempf, C. Han, P. Gamarachchi, D. Estrada, R. J. Mehta, Y. Zhang, *Sci. Rep.* **2016**, *6*, 33135.
- [15] S. J. Kim, J. H. We, B. J. Cho, *Energy Environ. Sci.* **2014**, *7*, 1959.
- [16] S. J. Kim, H. E. Lee, H. Choi, Y. Kim, J. H. We, J. S. Shin, K. J. Lee, B. J. Cho, *ACS Nano* **2016**, *10*, 10851.
- [17] H. W. Choi, T. Zhou, M. Singh, G. Jabbour, *Nanoscale* **2015**, *7*, 3338.
- [18] B. Y. Sun, J. A. Rogers, *Adv. Mater.* **2007**, *19*, 1897.
- [19] J. Y. Oh, J. H. Lee, S. W. Han, S. S. Chae, E. J. Bae, Y. H. Kang, W. J. Choi, S. Y. Cho, J.-O. Lee, H. K. Baik, T. Il Lee, *Energy Environ. Sci.* **2016**, *9*, 1696.
- [20] C. Dun, C. A. Hewitt, Q. Li, J. Xu, D. C. Schall, H. Lee, Q. Jiang, D. L. Carroll, *Adv. Mater.* **2017**, *29*, 1700070.
- [21] C. Wan, X. Gu, F. Dang, T. Itoh, Y. Wang, H. Sasaki, M. Kondo, K. Koga, K. Yabuki, G. J. Snyder, R. Yang, K. Koumoto, *Nat. Mater.* **2015**, *14*, 622.
- [22] S. H. Park, S. Jo, B. Kwon, F. Kim, H. W. Ban, J. E. Lee, D. H. Gu, S. H. Lee, Y. Hwang, J. S. Kim, D. Bin Hyun, S. Lee, K. J. Choi, W. Jo, J. S. Son, *Nat. Commun.* **2016**, *7*, 1.
- [23] C. Wan, R. Tian, M. Kondou, R. Yang, P. Zong, K. Koumoto, *Nat. Commun.* **2017**, *8*, 1024.
- [24] C. Dun, C. A. Hewitt, Q. Li, Y. Guo, Q. Jiang, J. Xu, G. Marcus, D. C. Schall, D. L. Carroll, *Adv. Mater.* **2017**, *29*, 1702968.
- [25] Y. Du, K. Cai, S. Chen, H. Wang, S. Z. Shen, R. Donelson, T. Lin, *Sci. Rep.* **2015**, *5*, 6411.
- [26] Y. Du, K. F. Cai, S. Chen, P. Cizek, T. Lin, *ACS Appl. Mater. Interfaces* **2014**, *6*, 5735.
- [27] Y. Wang, K. Cai, X. Yao, *ACS Appl. Mater. Interfaces* **2011**, *3*, 1163.
- [28] H. Song, K. Cai, *Energy* **2017**, *125*, 519.
- [29] Y. Du, J. Xu, B. Paul, P. Eklund, *Appl. Mater. Today* **2018**, *12*, 366.
- [30] C. Han, Q. Sun, Z. Li, S. X. Dou, *Adv. Energy Mater.* **2016**, *6*, 1600498.
- [31] F. R. Fan, W. Tang, Z. L. Wang, *Adv. Mater.* **2016**, *28*, 4283.
- [32] J.-H. Bahk, H. Fang, K. Yazawa, A. Shakouri, *J. Mater. Chem. C* **2015**, *3*, 10362.
- [33] J. Perelaer, P. J. Smith, D. Mager, D. Soltman, S. K. Volkman, V. Subramanian, G. Korvink, U. S. Schubert, *J. Mater. Chem.* **2010**, *20*, 8446.
- [34] H. Zhang, J. S. Son, D. S. Dolzhnikov, A. S. Filatov, A. Hazarika, Y. Wang, M. H. Hudson, C. J. Sun, S. Chattopadhyay, D. V. Talapin, *Chem. Mater.* **2017**, *29*, 6396.
- [35] J. S. Son, H. Zhang, J. Jang, B. Poudel, A. Waring, L. Nally, D. V. Talapin, *Angew. Chem., Int. Ed.* **2014**, *53*, 7466.
- [36] B. Poudel, Q. Hao, Y. Ma, Y. Lan, A. Minnich, B. Yu, X. Yan, D. Wang, A. Muto, D. Vashaee, X. Chen, J. Liu, M. S. Dresselhaus, G. Chen, Z. Ren, *Science* **2008**, *320*, 634.
- [37] Y. Liu, Y. Zhang, S. Ortega, M. Ibáñez, K. H. Lim, A. Grau-Carbonell, S. Martí-Sánchez, K. M. Ng, J. Arbiol, M. V. Kovalenko, D. Cadavid, A. Cabot, *Nano Lett.* **2018**, *18*, 2557.
- [38] Y. M. Kim, R. Lydia, J. Kim, C. Lin, K. Ahn, J. Rhyee, *Acta Mater.* **2017**, *135*, 297.

- [39] G. A. Slack, in *CRC Handbook of Thermoelectrics* (Ed. D. M. Rowe), CRC Press, Boca Raton, FL, USA **1995**, pp. 407–440.
- [40] L. Wang, Z. Zhang, Y. Liu, B. Wang, S. Wang, *Nat. Commun.* **2018**, *9*, 3817.
- [41] B. A. Macleod, N. J. Stanton, I. E. Gould, D. Wesenberg, R. Ihly, Z. R. Owczarczyk, K. E. Hurst, C. S. Fewox, C. N. Folmar, H. Hughes, B. L. Zink, L. Blackburn, A. J. Ferguson, *Energy Environ. Sci.* **2017**, *10*, 2168.
- [42] N. Toshima, K. Oshima, H. Anno, T. Nishinaka, S. Ichikawa, A. Iwata, Y. Shiraishi, *Adv. Mater.* **2015**, *27*, 2246.
- [43] G.-H. Kim, L. Shao, K. Zhang, K. P. Pipe, *Nat. Mater.* **2013**, *12*, 719.
- [44] C. Yang, D. Souchay, M. Kneiß, M. Bogner, H. M. Wei, M. Lorenz, O. Oeckler, G. Benstetter, Y. Q. Fu, M. Grundmann, *Nat. Commun.* **2017**, *8*, 16076.
- [45] B. Paul, E. M. Bjo, A. Kumar, J. Lu, P. Eklund, *ACS Appl. Energy Mater.* **2018**, *1*, 2261.
- [46] P. Lea, *Internet of Things for Architects*, Packt Publishing, Birmingham, UK **2018**.
- [47] S. K. Yee, S. LeBlanc, K. E. Goodson, C. Dames, *Energy Environ. Sci.* **2013**, *6*, 2561.